Journal of Materials Research and Technology 30 (2024) 8805–8814

Contents lists available at ScienceDirect

Journal of Materials Research and Technology

journal homepage: www.elsevier.com/locate/jmrt

Effect of design parameters on auxetic behavior and stiffness of additively manufactured 316L stainless steel

Mahmoud Khedr [a,b,*], Hassan Elshokrofy [a], Aki-Petteri Pokka [c], Atef Hamada [b], Matias Jaskari [b], Aappo Mustakangas [b], Antti Järvenpää [b], Abdelkader Ibrahim [a], Mahmoud Elsamanty [a,d,**]

[a] Mechanical Engineering Department, Faculty of Engineering at Shoubra, Benha University, Cairo, 11629, Egypt
[b] Kerttu Saalasti Institute, Future Manufacturing Technologies (FMT), University of Oulu, Nivala, FI, 85500, Finland
[c] Materials and Mechanical Engineering, University of Oulu, P.O. Box 4200, Oulu, 90014, Finland
[d] Mechatronics and Robotics Department, School of Innovative Design Engineering, Egypt-Japan University of Science and Technology, Alexandria, Egypt

ARTICLE INFO

Handling Editor: L Murr

Keywords:
Negative Poisson's ratio
Laser powder bed fusion
Finite element analysis
Digital image correlation
Strut thickness
Re-entrant orientation angle

ABSTRACT

Auxetic structures, characterized by showing negative Poisson's ratio (υ) when loaded, are cellular metamaterials consisting of connected struts in repeating unit cells. The mechanical behavior of auxetics depends on dimensions of the unit cell such as height and length of the unit cell, strut thickness (St), and orientation angle (θ) of the struts. The present study investigates effects of variations in St and θ on υ and stiffness (E) of additively manufactured 316L stainless steel with re-entrant honeycomb auxetics fabricated by laser powder bed fusion technique. Poisson's ratio was acquired through linear elastic simulations via finite element analysis (FEA) and verified experimentally through digital image correlation (DIC) facility attached to tensile tests. The design of the auxetic patterns entailed a simulation of thirty-five distinct models, incorporating St values of 0.4–1.6 mm, as well as θ values of 70–90°. In comparison, experimental validation was conducted on nine specimens, featuring St values of 0.6–1.4 mm, and θ values of 70–80°. FEA and experimental results obtained by DIC exhibited υ values of −5.23 to −0.3 (for St 0.6-1.4 mm and θ 70–80°), displaying increased υ with reductions in both St and/or θ. Meanwhile, E increased with St increase or θ decrease, exhibiting values of 18.9–72 GPa, which could be optimized to fit with human bones stiffness as potential orthopedics implantation in future.

1. Introduction

Auxetics are advanced lightweight cellular materials with great potential for energy absorption due to their superior damping characteristics [1,2]. Therefore, auxetic structures present promising prospects for a wide range of fields such as medical connections for myocardial infarction, bone scaffolds, acoustic insulation, cementitious reinforcements, and miscellaneous structural applications [3–7]. Auxetics, featuring negative Poisson's ratio, offer promising combinations of lightweight properties coupled with high strength and toughness [8]. This is attributed to their superior load-bearing capacity and outstanding dynamic performance [9–12]. Despite the superior mechanical response of auxetics, categorizing as metamaterials, investigations on auxetics as potential medical implants are scarce.

Regarding biomedical applications, many literatures investigated the production of lattice structures with porous sections having stiffness of approximately 20 GPa, close to human bones stiffness, via additive manufacturing [13–15]. However, a fabrication of low stiffness auxetics with three dimensional geometries via traditional manufacturing techniques, such as closed-cell metal foaming and lost wax casting [16,17], is challenging. Therefore, recent research endeavors to employ additive manufacturing (AM) techniques to fabricate intricate auxetics having lightweight high-strength characteristics [18].

The tensile behavior of auxetics is rarely reported in the open literature. Additionally, optimization of additively manufactured 316L stainless steel auxetics having low stiffness close to human bones is also scarce. There exists a significant gap in the literature regarding the production of re-entrant auxetic patterns in the 3D form via laser powder bed fusion (LPBF) [19–22]. Motivating us for this study, to reveal the evolution of Poisson's ratio (υ) as well as stiffness (E) during tensile testing of 3D printed auxetics at different wall-thicknesses (St) and re-entrant orientation angles (θ).

* Corresponding author. Mechanical Engineering Department, Faculty of Engineering at Shoubra, Benha University, Cairo, 11629, Egypt.
** Corresponding author. Mechanical Engineering Department, Faculty of Engineering at Shoubra, Benha University, Cairo, 11629, Egypt.
E-mail addresses: mahmoud.khedr@feng.bu.edu.eg, mahmoud.khedr@oulu.fi (M. Khedr), mahmoud.alsamanty@feng.bu.edu.eg (M. Elsamanty).

https://doi.org/10.1016/j.jmrt.2024.05.197
Received 30 April 2024; Received in revised form 21 May 2024; Accepted 22 May 2024
Available online 27 May 2024

316L stainless steel (SS) was selected to be investigated in this study due to its high corrosion resistance and extraordinary strength and ductility [23,24]. 316L-SS is characterized by their relatively high modulus of elasticity (~200 GPa), which is not compatible with human bones stiffness, however it can be manipulated when employed in an optimized auxetic structure through manipulations of the design parameters [25]. Therefore, the present study reveals the effect of variations in St and θ on υ and E of 316l SS with auxetic structures fabricated by LPBF. The study implies simulations via finite element analysis (FEA) and experimental verification of υ and E during tensile testing.

2. Experimental work

2.1. Design parameters

Three distinct sets of auxetic structures have been formulated, each comprising three individual designs characterized by varied thicknesses (St) of 0.6, 1.0, and 1.4 mm, while maintaining identical θ angles. The θ angles for the three groups are specified as 70, 75, and 80°, respectively. A 2D depiction of the re-entrant structure is presented in Fig. 1(a). Here, θ, L, and H denote the re-entrant orientation angle, the length, and the width of the designed auxetic unit cell, respectively.

Fig. 1(b) displays a schematic drawing of a unit cell of the auxetic pattern in the 3D form, the thickness of the extruded pattern is defined as the wire diameter or strut thickness (St). Notably, the auxetic pattern formed after the repetition of unit cells in 3D. Dimensions of L and H were kept constant with values of 6 and 4 mm, respectively. Values of St and θ were manipulated to investigate their effect on the mechanical behavior of the structures.

Table 1 displays dimensions of the experimental auxetic patterns with structures categorized based on St and θ. For example, the first set of structures designed with a consistent θ of 70° and varying St values (0.6, 1.0, and 1.4 mm) consists of three structures denoted as AUX70–0.6, AUX70–1.0, and AUX70–1.4. The selected dimensions of the experimental specimens were based on the buildability of the auxetic patterns via the LPBF machine, since horizontal struts have limitations on length as it may be broken during printing, similarly very thin struts might not form properly. Table 1 lists the minimum cross-sectional area and the corresponding density of the structures. Evidently, at the same strut thickness, with the increase in θ, the density of the structures is slightly decreased.

2.2. Powder properties and 3D printing parameters

The 316L SS powder used for the printing was provided by Lübeck company, Germany. The printing process was carried out by a selective laser melting (SLM) machine, SLM 280HL LPBF (SLM Solutions, Lübeck, Germany). The LPBF parameters include variable laser power and scan speed. The power and scanning speed of the laser beam depends on the location of the printed area, for instance, the borders of the specimens were carried out at laser power and scanning speed of 100 W and 0.4 m/s, respectively. Hatch distance and thickness of the printed layer were kept constant at 0.12 mm and 0.03 mm, respectively. Hatching lines were printed at laser power and scanning speed of 200 W and 0.8 m/s, respectively. Border lines were processed at a scan speed lower than the hatching profiles, to improve surface quality and provide higher strength of the outer skin, as reported in the literature [26–28]. In addition, the consumed energy density during the printing process was kept constant at a value of approximately 70 J/m^3.

2.3. Tensile testing and strain measurements by DIC

The printed auxetic specimens had a parallel length of 25 mm and a side width of 12 mm, with solid end gripping sides as shown in Fig. 2. The cross-sectional areas are 4.80, 12.96, and 24.96 mm^2 for 0.6, 1.0, and 1.4 mm thicknesses, respectively. The tension tests were performed by Zwick/Roell (Model: Z100) tension test machine at a strain rate of 10^{-3} s^{-1}. An extensometer with a gauge length of 20 mm was attached to the sides of the specimen during tensile testing to record the displacement accurately.

In this study, DIC was employed to evaluate longitudinal and lateral strains of the auxetics during tensile tests at the elastic zone, thus comparing the auxetic behavior of the printed samples with the simulation results. The tensile specimens were painted with a black-and-white speckle pattern, as seen in Fig. 3(a), to improve the DIC measurement reliability by providing a sufficient density of distinctive features on the surface and by minimizing glares. The tensile tests were recorded via a Lavision Strainmaster DIC system, equipped with two monochrome CCD cameras with a resolution of 2456 × 2058 pixels, as displayed in Fig. 3(b). DaVis 8.4 software was employed for digital image processing. This software uses an iterative least squares matching (LSM) algorithm based on optical flow estimation for calculating the full-field displacement of the specimen surface, enabling the determination of specimen dimensions changes during the tensile test. The recording and processing parameters for the DIC measurement are presented in Table 2.

Subsequently, axial and transverse strains were computed during the tensile tests through the tracking method by comparing these after-loading measurements to the initial image dimensions as a reference, utilizing equations (1)–(3), as follows:

$$\varepsilon_{\text{longitudinal}} = \frac{\text{final longitudinal length} - \text{initial longitudinal length}}{\text{initial longitudinal length}} \quad \text{eq. (1)}$$

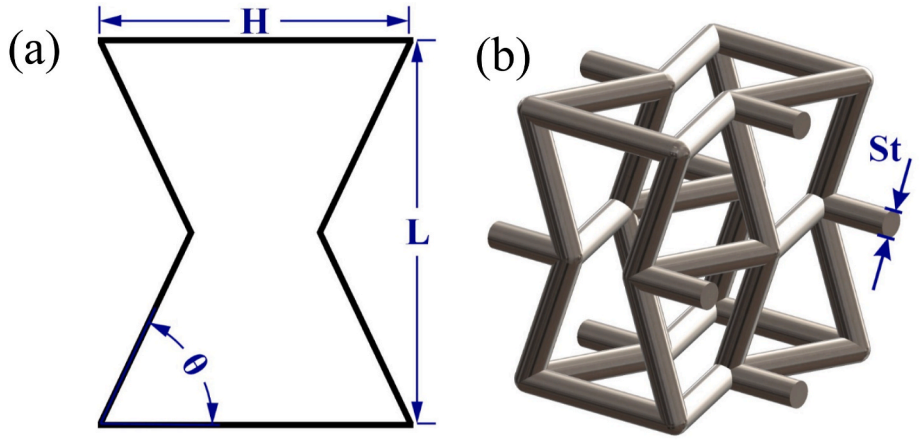

Fig. 1. (a) Basic dimensions of the auxetic structure in 2D, (b) 3D view of the re-entrant unit cell.

Table 1
Dimensions of the 3D printed experimental specimens.

Structure	Strut thickness St, mm	Orientation angle θ, deg	Cell height L, mm	Cell width H, mm	Min. cross sectional area, mm^2	Structure Density, $g.cm^{-3}$
AUX70–0.6	0.6	70	6	4	4.80	0.512
AUX70–1.0	1.0				12.96	1.320
AUX70–1.4	1.4				24.96	2.376
AUX75–0.6	0.6	75			4.80	0.504
AUX75–1.0	1.0				12.96	1.288
AUX75–1.4	1.4				24.96	2.328
AUX80–0.6	0.6	80			4.80	0.496
AUX80–1.0	1.0				12.96	1.272
AUX80–1.4	1.4				24.96	2.304

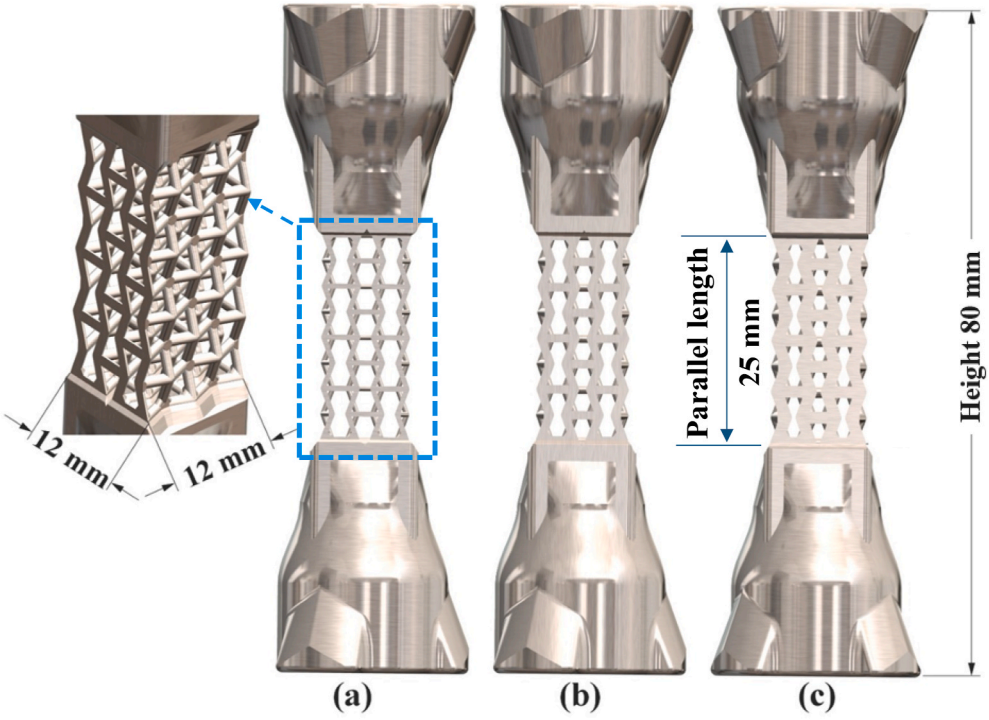

Fig. 2. Schematic drawings of tension test specimens with auxetic patterns having different wall-thicknesses: (a) St = 0.6 mm, (b) St = 1.0 mm, and (c) St = 1.4 mm, and a magnified view showing the gauge area in the 3D.

$$\varepsilon_{lateral} = \frac{\text{final lateral length} - \text{initial lateral length}}{\text{initial lateral length}} \quad \text{eq. (2)}$$

$$\upsilon = -\frac{\varepsilon_{x-2\to5}}{\varepsilon_{y-1\to3}} \quad \text{eq. (3)}$$

Poisson's ratio was calculated from lateral and longitudinal strains $\varepsilon_{lateral}$ and $\varepsilon_{longitudinal}$, respectively, which are estimated from equations (1) and (2) and substituted in equation (3). The term $\varepsilon_{(x\text{-}2\to5)}$ represented the value of lateral strain calculated in X-axis direction between points 2 and 5 and. The term $\varepsilon_{(y\text{-}1\to3)}$ represented the value of longitudinal strain calculated in Y-axis direction between points 1 and 3, as shown in Fig. 3 (a). The experimental values of υ were compared with the simulated ones to validate the auxetic behavior of the specimens.

2.4. Finite element analysis (FEA)

FEA was employed to simulate the elastic behavior of the designed auxetics with a wide range of St (0.4, 0.6, 1.0, 1.4, and 1.6 mm) and θ (70, 75, 80, 85, 86, 89, and 90°). As an initial step, a CAD model was built for the 35 samples using SOLIDWORKS software, to prepare the geometry file for each specimen. After geometry preparation, ANSYS software was employed to perform the FEA process to study the effect of the different geometrical parameters on values of Poisson's ratio of the structures.

2.4.1. Boundary conditions

The boundary conditions are chosen in such a way that could be applied for the estimation of υ values through both simulation analysis and experimental calculation. Therefore, a frictionless support is applied at the bottom surface of the specimen to ensure that the surface is fixed at Y-axis direction and free to slide in X- and Z-axes directions when a normal displacement is applied at the free end along the longitudinal direction (Y-axis). This configuration ensures that all points in the unit cell can deform without any external constraints, as reported by Xiong et al. [29]. A meshing procedure was conducted on the model, with an element size of 0.5 mm. This mesh discretization ensures a precise representation of the specimen geometry and facilitates the analysis of strain and deformation distribution.

2.4.2. Calculation of Poisson's ratio

Values of the lateral strain (εx) and longitudinal strain (εy) were extracted from simulation results according to eq. (4) and eq. (5), through computing of the displacement in X (Δx) and Y (Δy) axes. Thus,

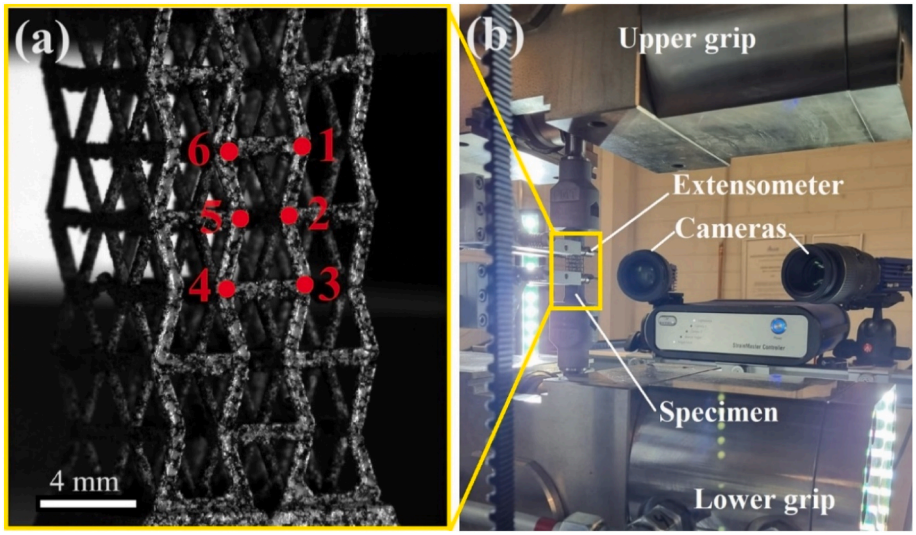

Fig. 3. (a) A sprayed tension test specimen during DIC capturing exhibiting the six reference points tracked for calculating the displacement within the gauge area, (b) the experimental setup of the tensile tests recording via the Lavision Strainmaster DIC system used for full-field displacement measurement.

Table 2
DIC recording and processing parameters during tensile tests.

DIC system	**Lavision Strainmaster (Stereo DIC)**
Sensor, resolution and digitization	CCD, 2456 × 2058 pixels, 12-bit
Lens, imaging distance	100 mm C-mount, 0.41 m
Imaging rate	2 Hz
Subset size	31 × 31 pixels
Step size	11 pixels
Strain window, smoothing method	5 × 5 data points, 2nd order polynomial fit
Virtual strain gage size	75 pixels
Image scale	90 pixels/mm
Displacement resolution	0.16 μm
Interpolation, shape function, algorithms	6th order spline interpolation; quadratic shape function; LSM algorithm

the values of Poisson's ratio were calculated according to eq. (6), as follows:

$$\varepsilon y = \Delta y / ly \quad \text{eq. (4)}$$

$$\varepsilon x = \Delta x / lx \quad \text{eq. (5)}$$

$$\upsilon = -\varepsilon x / \varepsilon y \quad \text{eq. (6)}$$

where ly and lx are the initial indices of the tracked points along X and Y directions during the simulations via the ANSYS software.

Fig. 4 shows a schematic drawing of the boundary conditions applied to carry out the calculations of υ via FEA. The boundary conditions imply a fixed support at the bottom surface of the sample at position B (fixed end), while the applied load is located on the opposite side of the specimen at position A (free end). To track the strain in both lateral (X-axis) and longitudinal (Y-axis) directions, the indices of six points at the corners of the middle unit cell (chosen as reference points) were recorded at different loading values during the elastic deformation of the

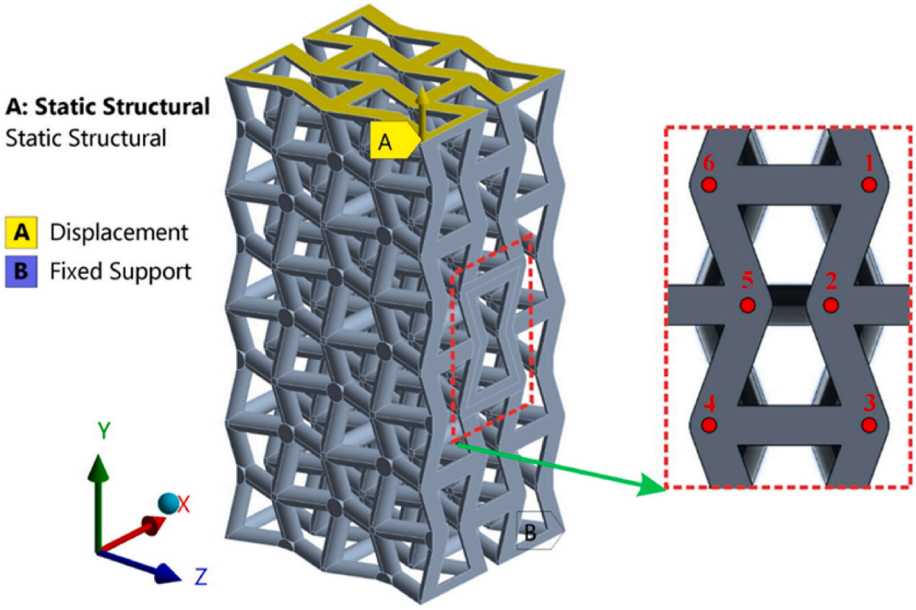

Fig. 4. Boundary condition set for the FEA model.

models, as shown in Fig. 4. The specimens were subjected to a maximum displacement of 0.02 mm during the simulation, to ensure that the induced stress remained below the material's yield strength, which is specified at 300 MPa. This controlled loading condition allowed for a precise examination of the mechanical response of the specimens, enabling accurate assessment of their elastic behavior while avoiding any plastic deformation that could influence the calculated Poisson's ratio.

3. Results and discussion

3.1. Tensile testing

Fig. 5 shows stress-strain curves of the printed auxetic specimens with different St and θ, as well as the corresponding values of the yield and ultimate tensile strengths. Clearly, the strength and ductility of the investigated auxetics are decreased with thickness decrease. Since auxetics with 0.6 mm thickness exhibited low strength values as compared to specimens with 1.0- and 1.4-mm thicknesses, due to deterioration of surface roughness and promotion of printing defects with wall-thickness reduction [30–33].

AUX-0.6 exhibited yield strength (YS) and ultimate tensile strength (UTS) of 109–118 MPa and 334–340 MPa, respectively. AUX-1.0 displayed respective YS and UTS of 255–305 MPa and 461–485 MPa. AUX-1.4 showed YS and UTS of 350–385 MPa and 537–552 MPa, respectively.

On the other hand, in auxetics having same St, with θ increase, both YS and UTS are slightly increased. For instance, at St of 1.0 mm, auxetics with θ equals 70, 75, and 80° (AUX70–1.0, AUX75–1.0, and AUX80–1.0) depicted YS of 255 ± 50, 278 ± 35, and 305 ± 30 MPa and UTS of 461 ± 30, 473 ± 20, and 485 ± 15 MPa, respectively.

Notably, the stress-strain curves display serrated flow, which starts at earlier strain levels with St reduction. The appearance of those serrations is attributed to premature failure of the struts (see supplementary videos of DIC facility). Struts failure is attributed to elevated stress concentration at nodes intersections, in agreement with the literature [34] reporting expedited struts failure in thin-walled sections. Despite variation in St and θ, ductility of the printed auxetics displayed close proximity ranging between 30 and 36%.

Poisson's ratio of the specimens undergone the tensile testing was obtained by processing the images recorded by the DIC facility through the tracking method of the middle unit cell edges, as illustrated in Fig. 3 (a), via eqs (1)–(3). The recorded DIC videos are provided in the supplementary materials. Table S1 (see the supplementary material) displays values of lateral and transverse strains employed in the calculations of υ.

Fig. 6 exhibits the effect of variations in St and θ on values of υ and E. It was found that with the thickness increase, υ was dramatically decreased. For instance, auxetic specimens having θ = 70° displayed υ values of −5.23, −2.14, and −1.11, at St = 0.6, 1.0, and 1.4 mm, respectively. In addition, auxetics with θ = 80°, υ measured −4.15, −2.67, and −1.01, at St = 0.6, 1.0, and 1.4 mm, respectively. The present results of υ agree with the findings presented recently by Afdhal et al. [35] who found that the auxetic behavior is promoted with the thickness reduction due to the decrease of the struts infill percentage, since the thinner struts result in an increase of the lattice porosity, which provides enough space for an enhanced lateral deformation. Despite υ values are intensively affected by St change, variations in θ have a little effect on υ.

The auxetic structures with 0.6 mm wall thicknesses display slight decrease of υ with θ increase, since at θ = 70, 75, and 80°, υ measured −5.23, −4.84, and −4.15, respectively. It can be concluded that the auxetic behavior is inversely proportional to θ increase. Even though the specimens with 1.0- and 1.4-mm wall thicknesses displayed values of υ in close proximity at different θ, showcasing respective υ values around −2.14 to −2.67 and −1.36 to −1.01.

Fig. 6 b depicts the effect of design parameters variation on modulus of elasticity. The stiffness of the specimens is decreased whether with St decrease or θ increase. The minimum E (18.9 ± 4 GPa) was found at St of 0.6 mm and θ of 80°, whereas the maximum E (72 ± 3 GPa) was found at

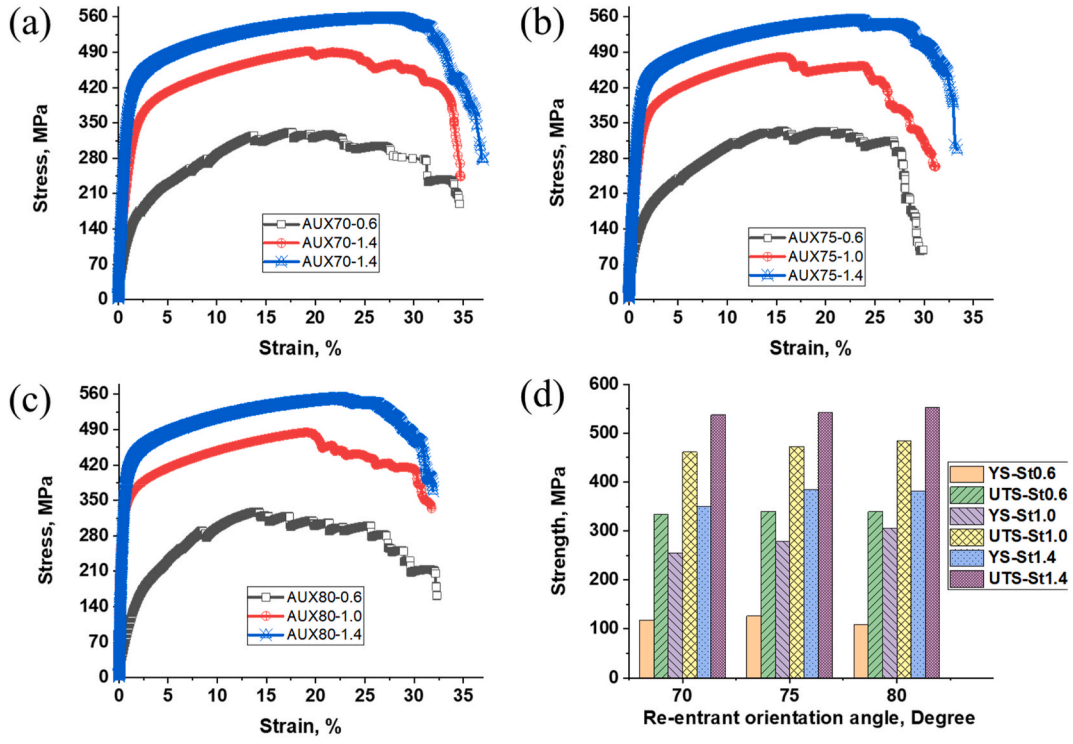

Fig. 5. The stress-strain curves of the printed specimens with different St (0.6, 1.0, and 1.4 mm) and different θ: (a) 70°, (b) 75°, (c) 80°, and (d) the corresponding YS and UTS.

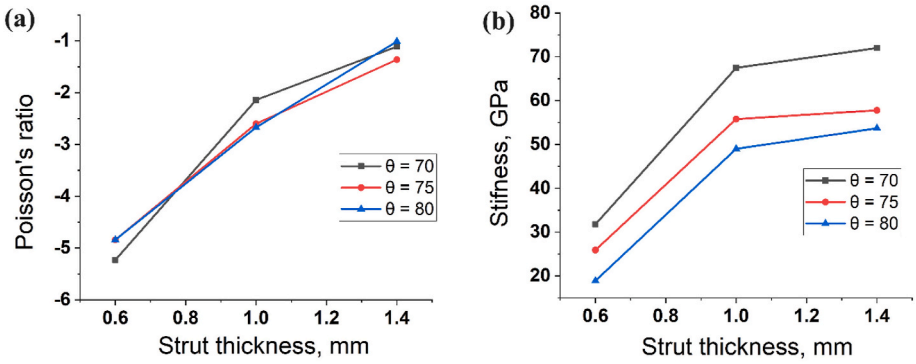

Fig. 6. Effects of variations in St on the evolution of (a) Poisson's ratio and (b) stiffness at different θ.

St of 1.4 mm and θ of 70°.

3.2. Stresses acting on struts due to variations in wall-thickness and re-entrant angle

During tensile testing, axial, shear, and bending stresses affect the mechanical behavior of auxetic specimens due to struts inclination [36, 37]. The value of the re-entrant orientation angle determines the effective stress acting on the struts to some extent, which directly affects the corresponding values of υ and E.

Fig. 7 shows a schematic drawing of the forces acting on a strut in a unit cell. F_{st} represents the normal force acting on the strut, it can be resolved into two components along horizontal and vertical directions. Clearly, the value F_{st}*Sin(θ) initiates axial stress in the strut, while the component F_{st}*Cos(θ) induces transverse shear and bending stress with a bending arm of L/2*Sin(θ), by assuming a henge support condition at the node's intersections of the struts. Axial (σ_a), shear (τ) and bending (σ_b) stresses can be calculated according to equations 7, 8, and 9 as follows:

$$\sigma_a = \frac{F}{A} = \frac{F_{st}\ Sin(\theta)}{\frac{\pi}{4}d^2} = \frac{4\ F_{st}\ Sin(\theta)}{\pi d^2} \quad \text{Eq (7)}$$

$$\tau = \frac{VQ}{Ib} = \frac{4V}{3A} = \frac{4\ F_{st}\ Cos(\theta)}{3\frac{\pi}{4}d^2} = \frac{16\ F_{st}\ Cos(\theta)}{3\ \pi d^2} \quad \text{Eq (8)}$$

$$\sigma_b = \frac{MC}{I} = \frac{F_{st}\ Cos(\theta) \times \frac{L}{2\ Sin(\theta)} \left(\frac{d}{2}\right)}{\frac{\pi}{64}d^4} = \frac{16\ F_{st}\ Cos(\theta) \times L}{\pi Sin(\theta) d^3} \quad \text{Eq (9)}$$

Clearly, variations in θ have little effect on σ_a, since Sin(70) and Sin(80) equal 0.94 and 0.98, respectively, which shows a limited increase in the axial stress with θ increase. Despite θ severely affecting τ and σ_b, since at θ = 70°, Cos(θ) = 0.34, whereas at θ = 80°, Cos(θ) = 0.17. Therefore, at θ = 80°, τ and σ_b are decreased by half the value at θ = 70° of the specimens having the same wall-thicknesses. At the same time, values of τ are very small, it can be neglected in comparison with σ_a and σ_b. On the other hand, σ_b is inversely proportional to the moment of inertia (I). At St-0.6, St-1.0, and St-1.4, I equal 6.4×10^{-3}, 49.1×10^{-3}, and 188.7×10^{-3} mm^4, respectively. Consequently, with St reduction, σ_b is magnified. Therefore, the increasing bending stress acting on the struts results in rising of υ due to enhancing the lateral extension of the struts (in the transverse direction), but reduced E due to lower resistance of the structure to the bending effect induced by the tangential component (F_{st}*Cosθ).

By taking into consideration values of YS and UTS of the printed auxetics with the same thickness but different θ, we find that at St = 1.4 mm and θ of 70 and 80°, YS measured 350 and 382 MPa, respectively. Furthermore, at St = 1.0 mm with θ = 70 and 80°, UTS measured 461 and 485 MPa, respectively. Thus, at lower θ values, struts are vulnerable to failure due to bending effect being greater than axial stress, which decreases the strength of the auxetics with reductions in θ.

3.3. FEA

Fig. 8 displays the effect of changing St on the auxetic behavior of the designed specimens at the same orientation angle (θ = 70°) through FEA via ANSYS software program. The specimen with St of 0.4 mm displayed a maximum lateral displacement of 0.014 mm (at X-direction), whereas

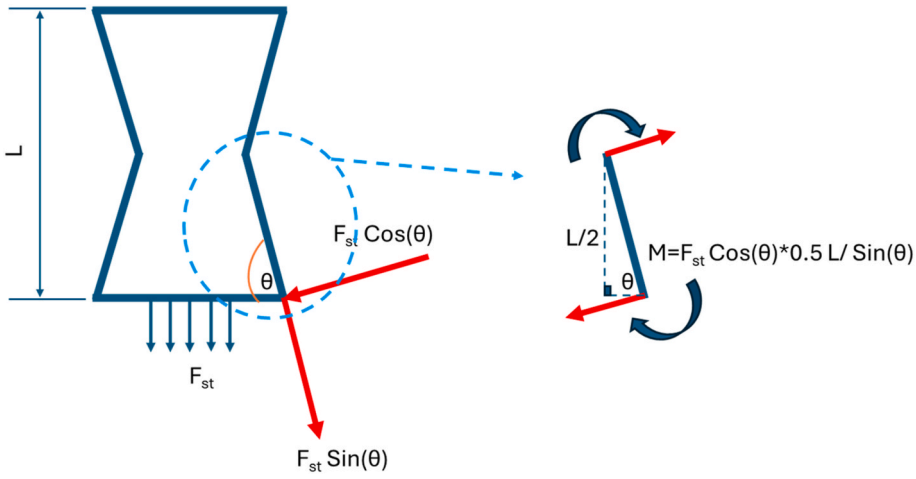

Fig. 7. Forces acting on an inclined strut with angle θ during tensile testing.

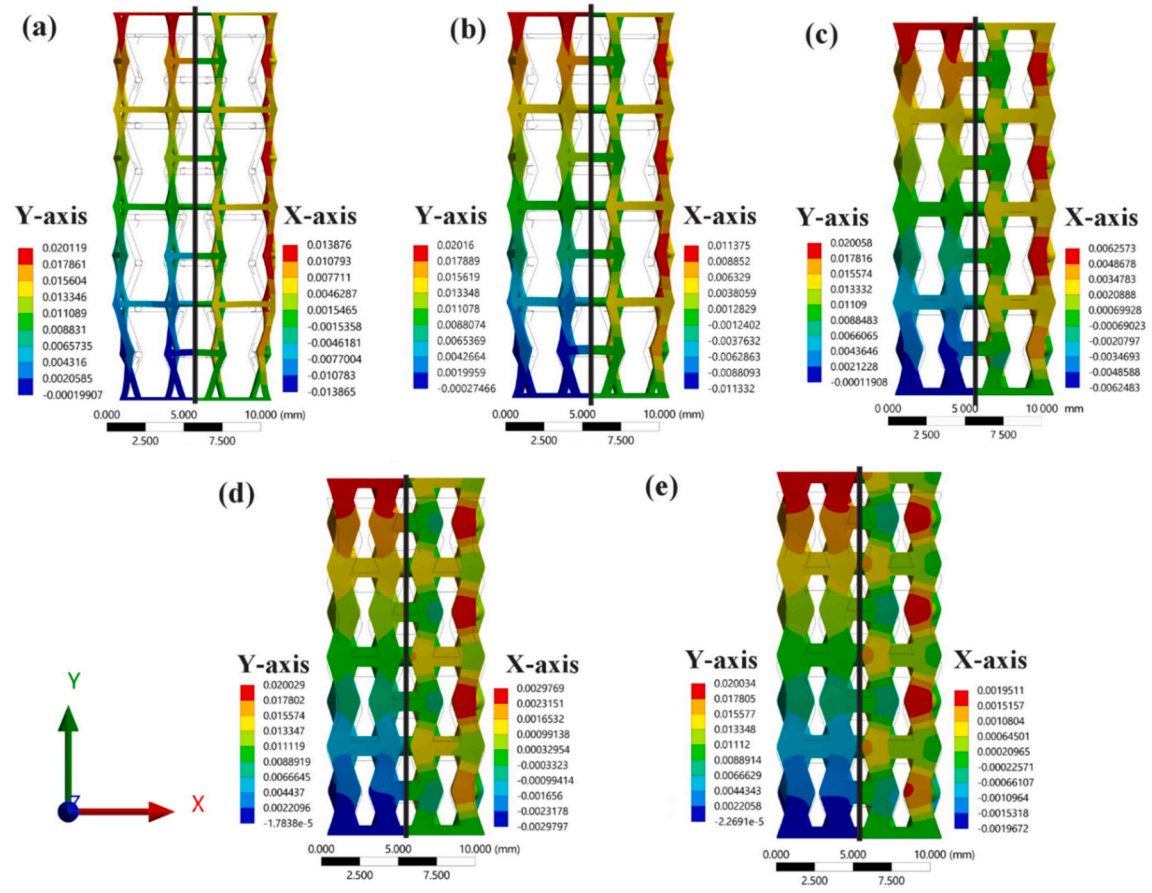

Fig. 8. The effect of strut thickness increases on lateral displacements via FEA. The simulated specimens have θ = 70° and different St: (a) 0.4 mm, (b) 0.6 mm, (c) 1 mm, (d) 1.4 mm, and (e) 1.6 mm. The colored figures represent auxetic structures at a maximum longitudinal displacement of 0.02 mm, while the shadows in the background refer to the rest position.

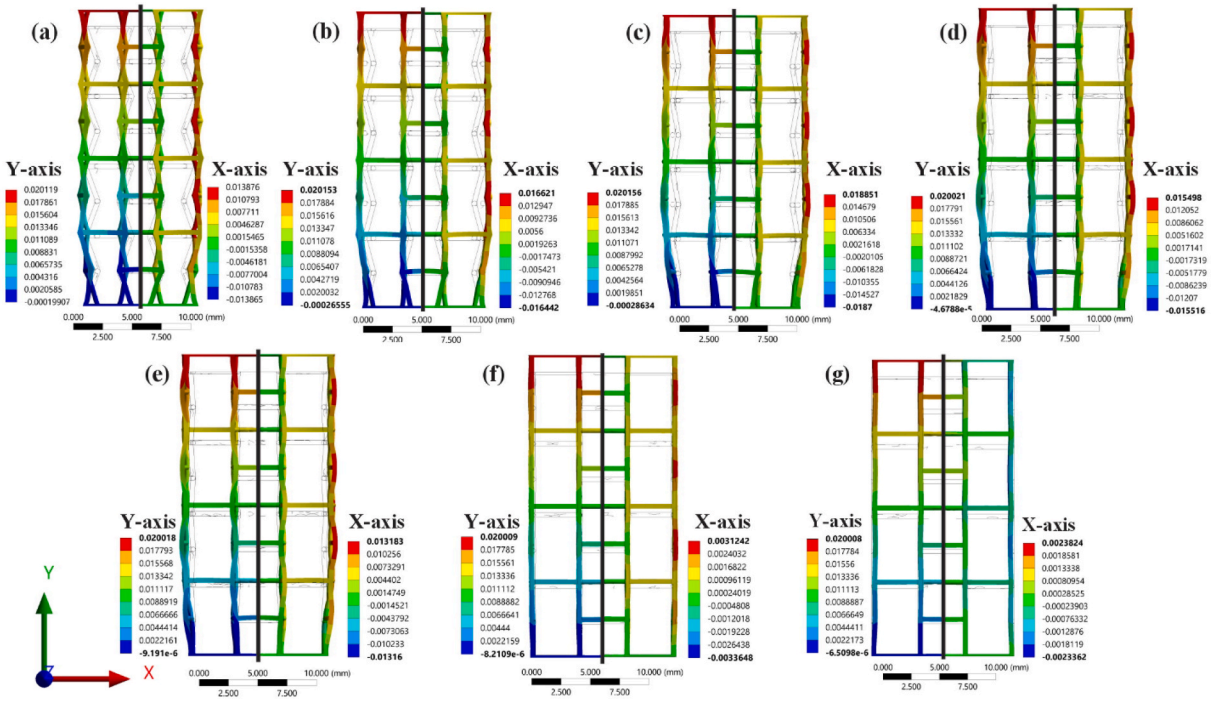

Fig. 9. The effect of orientation angle increases on the lateral displacement via FEA. The simulated specimens have St = 0.4 mm and different θ: (a) 70°, (b) 75°, (c) 80°, (d) 85°, (e) 86°, (f) 89°, and (g) 90°. The colored figures represent auxetic structures at a longitudinal displacement of 0.02 mm, while the shadows in the background refer to the rest position. (Colored figure).

the specimen with 1.6 mm thickness exhibited a maximum lateral displacement of 0.002 mm. Clearly, the rise in St values results in a decreased lateral deformation. Despite the longitudinal deflections were kept at the same values (0.02 mm), the lateral displacements were decreased with St increase, see the simulation video "FEA St variation" in the supplementary material.

The FEA findings indicate that the increase in St leads to a drop in Poisson's ratio values at the same re-entrant orientation angle, displaying hindered auxetic behavior with the St rise, due to thickening of the connecting zones between the struts which makes it stiffer. Consequently, the rotation of the struts responsible for increasing the lateral strain is significantly hindered, resulting in a reduced auxetic behavior.

Fig. 9 shows the influence of increasing θ on the lateral deformation under a longitudinal displacement of 0.02 mm at the same St (0.4 mm) via FEA. Lateral deformation is decreased with the orientation angle increase, since the maximum lateral deformation recorded 0.013 mm and 0.003 mm at θ = 70 and 89°, respectively. Furthermore, at θ = 90°, the lateral displacement was negative, recording −0.0003 mm in the middle unicell, corresponding to a positive υ of 0.37.

Fig. 10 summarizes the impact of the increase in orientation angle on the values of Poisson's ratio at various St values for the 35 specimens, as determined through FEA. Clearly, both an increase in θ or St results in a reduction of the auxetic behavior exhibited by the designed models, which agrees with the findings in the literature [38,39]. Notably, specimens with the lowest strut thickness (St = 0.6 mm) and varying θ values exhibit the highest Poisson's ratio (υ) values. Furthermore, when θ reaches 90°, the specimens demonstrate positive values of υ, indicating non-auxetic behavior. This is attributed to the elimination of lateral displacement with the increase of θ or St, as elucidated in the supplementary materials' videos titled "FEA St variation" and "FEA Theta Variation". Furthermore, with θ increase from 70 to 80°, υ is slightly increased in agreement with the experimental results of υ presented in Fig. 6 (a).

3.4. Validation of υ

In this section, a comparison of υ values obtained by experiments and FEA is carried out. The captured videos via DIC during the tensile testing as well as the corresponding simulation results of the auxetic specimens are provided in the supplementary materials. Fig. 11 showcases υ values obtained by FEA combined with the experimental results obtained by DIC. The experimental results exhibit that with the thickness reduction of the specimens, the auxetic behavior is enhanced, which agrees with the simulation results. Furthermore, υ is decreased with the increase of the re-entrant orientation angle from 70 to 80°, which also is in agreement with the FEA results. Despite, there are slight differences between experiments and FEA. The auxetic specimens with a re-entrant

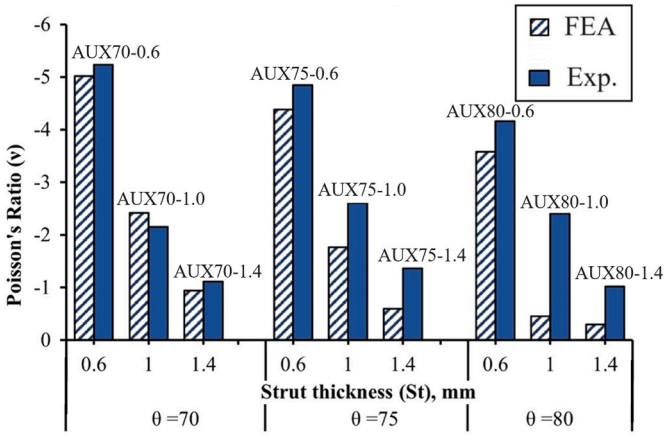

Fig. 11. Comparison of Poisson's ratio values obtained by FEA and experimental results.

orientation angle of 70° display a good agreement between simulation and experimental results more than the auxetic specimens with the orientation angle of 80° regardless of the sample thickness. Furthermore, the experimental results mostly display values greater than the simulation results. This confirms the enhancement of the lateral extension more than the longitudinal elongation during the tensile testing in all printed samples. This divergence in υ values obtained by FEA and experimental results is attributed to uncontrolled printing conditions, which randomly affect the quality of the printed struts such as their dimensions, in agreement with the literature [18,36]. Maran et al. [21] confirmed that the platform rotation angle during the printing process could randomly cause slight differences in the printed sample's dimensions from the corresponding values existing in the CAD files submitted to the FEA software, which randomly affects the displacement of the printed samples [21]. In addition, Novak et al. [40] concluded that the node's area of the auxetic structures display elastoplastic deformation under loading, which intensively affects the lateral strain values of the experimental specimens more than the simulation results. Resulting in variations between simulation and experimental results.

To sum up, the fabrication of 3D auxetic specimens through AM was successfully carried out via LPBF. There was a good agreement between experiments and simulations regarding Poisson's ratio values. However, the absolute strength of thin-walled sections was found to be unsatisfactory. Nonetheless, modulus of elasticity of the thin-walled auxetics displayed values comparable to the stiffness of human bones. Consequently, optimization of the printing parameters of various biomaterials, such as Ti6Al4V, should be considered for future investigations to leverage the mechanical behavior of thin-walled auxetics printed by

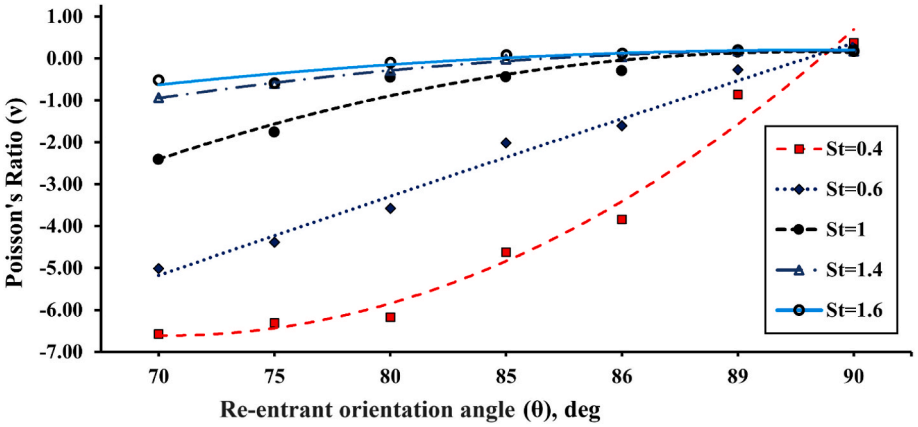

Fig. 10. The effect of variations in strut thickness (St) and re-entrant orientation angle (θ) on Poisson's ratio values as obtained by FEA.

LPBF, potentially for orthopedic implants.

4. Conclusions

In the present study, the manufacturing of 316L-SS featuring honeycomb auxetic structures with different thicknesses and orientation angles was conducted via the LPBF technique. υ was evaluated based on experimental results obtained via DIC facility and then compared with FEA. Both experimental and simulation results indicated that the auxetic behavior is enhanced with reductions in strut thickness or the re-entrant orientation angle. For example, experimental results showed that at St = 0.6 mm and θ = 70°, υ was −5.23, whereas at St = 1.4 and θ = 80°, υ recorded −1.02. Meanwhile, the respective FEA results displayed υ values of −5.02, and −0.29. Furthermore, the stiffness of the printed auxetics decreased with reductions in St or increases in θ. A minimum E of 18.9 GPa was achieved at St = 0.6 mm and θ = 80°, whereas a maximum E of 72 GPa was measured at St = 1.4 mm and θ = 70°, demonstrating promising optimizable stiffness for potential usages of honeycomb auxetics in implants fabrication.

Funding

The authors express their gratitude to the BUSINESS Finland for funding this research through “DREAMS” project, No. 4795/31/2021.

Data availability

Data will be made available on request.

Credit author statement

Mahmoud Khedr: Writing–original draft, Data curation, Validation, Formal analysis, Methodology, Investigation, Conceptualization, Supervision, Writing final draft– Review & Editing. Hassan Elshokrofy: Writing–original draft, Software, Investigation, Data curation, Validation, Formal analysis. Aki-Petteri Pokka: Methodology, Software, Investigation, Data curation, Validation, Editing. Atef Hamada: Review & Editing. Matias Jaskari: Methodology, Investigation. Aappo Mustakangas: Methodology, Software. Antti Järvenpää;: Funding acquisition, Project management, Resources. Abdelkader Ibrahim: Supervision, Visualization, Conceptualization. Mahmoud Elsamanty: Methodology, Formal analysis, Conceptualization, Validation, Supervision, Review & Editing.

Declaration of competing interest

The authors declare that they have no known competing financial interests or personal relationships that could have appeared to influence the work reported in this paper.

Acknowledgment

Mahmoud Khedr would like to express his sincere thanks for the financial support from the Finnish Foundation for Technology Promotion in Finland.

Appendix A. Supplementary data

Supplementary data to this article can be found online at https://doi.org/10.1016/j.jmrt.2024.05.197.

References

[1] Najafi M, Ahmadi H, Liaghat G. Experimental investigation on energy absorption of auxetic structures. Mater Today Proc 2021;34:350–5. https://doi.org/10.1016/j.matpr.2020.06.075.

[2] Wang Z. Recent advances in novel metallic honeycomb structure. Compos B Eng 2019;166:731–41. https://doi.org/10.1016/j.compositesb.2019.02.011.

[3] Wanniarachchi CT, Arjunan A, Baroutaji A, Singh M. Mechanical performance of additively manufactured cobalt-chromium-molybdenum auxetic meta-biomaterial bone scaffolds. J Mech Behav Biomed Mater 2022;134:105409. https://doi.org/10.1016/j.jmbbm.2022.105409.

[4] Wang Z, Zhou Y, Wang X, Wei K. Compression behavior of strut-reinforced hierarchical lattice—experiment and simulation. Int J Mech Sci 2021;210:106749. https://doi.org/10.1016/j.ijmecsci.2021.106749.

[5] Sun ZP, Guo YB, Shim VPW. Deformation and energy absorption characteristics of additively-manufactured polymeric lattice structures — effects of cell topology and material anisotropy. Thin-Walled Struct 2021;169:108420. https://doi.org/10.1016/j.tws.2021.108420.

[6] Bacigalupo A, De Bellis ML, Misseroni D. Design of tunable acoustic metamaterials with periodic piezoelectric microstructure. Extreme Mech Lett 2020;40:100977. https://doi.org/10.1016/j.eml.2020.100977.

[7] Gómez-Silva F, Zaera R. Low order nonstandard continualization of a beam lattice with next-nearest interactions: enhanced prediction of the dynamic behavior. Mech Adv Mater Struct 2022;29:6216–30. https://doi.org/10.1080/15376494.2021.1974616.

[8] Elsamanty M, Elshokrofy H, Ibrahim A, Järvenpää A, Khedr M. Investigation and tailoring of rotating squares’ and rectangles’ auxetic structure behavior through computational simulations of 6082T6 aluminum alloy structures. Materials 2023;16. https://doi.org/10.3390/ma16247597.

[9] Bronder S, Herter F, Röhrig A, Bähre D, Jung A. Design study for multifunctional 3D Re-entrant auxetics. Adv Eng Mater 2022;24:2100816. https://doi.org/10.1002/adem.202100816.

[10] Kelkar PU, Kim HS, Cho KH, Kwak JY, Kang CY, Song HC. Cellular auxetic structures for mechanical metamaterials: a review. Sensors 2020;20:1–26. https://doi.org/10.3390/s20113132.

[11] Evans AG, Hutchinson JW, Fleck NA, Ashby MF, Wadley HNG. The topological design of multifunctional cellular metals. Prog Mater Sci 2001;46:309–27. https://doi.org/10.1016/S0079-6425(00)00016-5.

[12] Tancogne-Dejean T, Diamantopoulou M, Gorji MB, Bonatti C, Mohr D. 3D plate-lattices: an emerging class of low-density metamaterial exhibiting optimal isotropic stiffness. Adv Mater 2018;30:1803334. https://doi.org/10.1002/adma.201803334.

[13] Benedetti M, du Plessis A, Ritchie RO, Dallago M, Razavi N, Berto F. Architected cellular materials: a review on their mechanical properties towards fatigue-tolerant design and fabrication. Mater Sci Eng R Rep 2021;144:100606. https://doi.org/10.1016/j.mser.2021.100606.

[14] Emanuelli L, Jam A, du Plessis A, Lora C, De Biasi R, Benedetti M, Pellizzari M. Manufacturability of functionally graded porous β-Ti21S auxetic architected biomaterials produced by laser powder bed fusion: comparison between 2D and 3D metrological characterization. Int J Bioprint 2023;9. https://doi.org/10.18063/ijb.728.

[15] Morgan EF, Unnikrisnan GU, Hussein AI. Bone mechanical properties in healthy and diseased states. Annu Rev Biomed Eng 2018;20:119–43. https://doi.org/10.1146/annurev-bioeng-062117-121139.

[16] Changdar A, Chakraborty SS. Laser processing of metal foam - a review. J Manuf Process 2021;61:208–25. https://doi.org/10.1016/j.jmapro.2020.10.012.

[17] Xue Y, Wang W, Han F. Enhanced compressive mechanical properties of aluminum based auxetic lattice structures filled with polymers. Compos B Eng 2019;171:183–91. https://doi.org/10.1016/j.compositesb.2019.05.002.

[18] Gao M, He D, Wu X, Tan Z, Guo X. Design, preparation, and mechanical property investigation of Ti–Ta 3D-auxetic structure by laser powder bed fusion. Adv Eng Mater 2023;25:2300242. https://doi.org/10.1002/adem.202300242.

[19] V Nguyen N, Nguyen-Xuan H, Nguyen TN, Kang J, Lee J. A comprehensive analysis of auxetic honeycomb sandwich plates with graphene nanoplatelets reinforcement. Compos Struct 2021;259:113213. https://doi.org/10.1016/j.compstruct.2020.113213.

[20] Novak N, Duncan O, Allen T, Alderson A, Vesenjak M, Ren Z. Shear modulus of conventional and auxetic open-cell foam. Mech Mater 2021;157:103818. https://doi.org/10.1016/j.mechmat.2021.103818.

[21] Maran S, Masters IG, Gibbons GJ. Additive manufacture of 3D auxetic structures by laser powder bed fusion—design influence on manufacturing accuracy and mechanical properties. Appl Sci 2020;10. https://doi.org/10.3390/app10217738.

[22] Delcuse L, Bahi S, Gunputh U, Rusinek A, Wood P, Miguelez MH. Effect of powder bed fusion laser melting process parameters, build orientation and strut thickness on porosity, accuracy and tensile properties of an auxetic structure in IN718 alloy. Addit Manuf 2020;36:101339. https://doi.org/10.1016/j.addma.2020.101339.

[23] Xu M, Guo H, Wang Y, Hou Y, Dong Z, Zhang L. Mechanical properties and microstructural characteristics of 316L stainless steel fabricated by laser powder bed fusion and binder jetting. J Mater Res Technol 2023;24:4427–39. https://doi.org/10.1016/j.jmrt.2023.04.069.

[24] Hamada A, Mansour EH, Jaskari M, Abd-Elaziem W, Mohamed AK, Elshokrofy H, Mustakangas A, Järvenpää A, Khedr M. Strengthening aluminum matrix composite with additively manufactured 316L stainless steel lattice reinforcement: processing methodology, mechanical performance and deformation mechanism. J Mater Res Technol 2024;29:1087–101. https://doi.org/10.1016/j.jmrt.2024.01.172.

[25] Yu A, Zhang C, Xu W, Zhang Y, Tian S, Liu B, Zhang J, He A, Su B, Lu X. Additive manufacturing of multi-morphology graded titanium scaffolds for bone implant applications. J Mater Sci Technol 2023;139:47–58. https://doi.org/10.1016/j.jmst.2022.07.035.

[26] Haghdadi N, Laleh M, Moyle M, Primig S. Additive manufacturing of steels: a review of achievements and challenges. J Mater Sci 2021;56:64–107. https://doi.org/10.1007/s10853-020-05109-0.
[27] Oliveira JP, LaLonde AD, Ma J. Processing parameters in laser powder bed fusion metal additive manufacturing. Mater Des 2020;193:108762. https://doi.org/10.1016/j.matdes.2020.108762.
[28] Narasimharaju SR, Zeng W, See TL, Zhu Z, Scott P, Jiang X, Lou S. A comprehensive review on laser powder bed fusion of steels: processing, microstructure, defects and control methods, mechanical properties, current challenges and future trends. J Manuf Process 2022;75:375–414. https://doi.org/10.1016/j.jmapro.2021.12.033.
[29] Xiong J, Mines R, Ghosh R, Vaziri A, Ma L, Ohrndorf A, Christ H-J, Wu L. Advanced micro-lattice materials. Adv Eng Mater 2015;17:1253–64. https://doi.org/10.1002/adem.201400471.
[30] Ahuja B, Schaub A, Karg M, Lechner M, Merklein M, Schmidt M. Developing LBM process parameters for Ti-6Al-4V thin wall structures and determining the corresponding mechanical characteristics. Phys Procedia 2014;56:90–8. https://doi.org/10.1016/j.phpro.2014.08.102.
[31] Niendorf T, Leuders S, Riemer A, Richard HA, Tröster T, Schwarze D. Highly anisotropic steel processed by selective laser melting. Metall Mater Trans B 2013;44:794–6. https://doi.org/10.1007/s11663-013-9875-z.
[32] Haghshenas A, Khonsari MM. Damage accumulation and crack initiation detection based on the evolution of surface roughness parameters. Int J Fatig 2018;107:130–44. https://doi.org/10.1016/j.ijfatigue.2017.10.009.
[33] Guo C, Li S, Shi S, Li X, Hu X, Zhu Q, Ward RM. Effect of processing parameters on surface roughness, porosity and cracking of as-built IN738LC parts fabricated by laser powder bed fusion. J Mater Process Technol 2020;285:116788. https://doi.org/10.1016/j.jmatprotec.2020.116788.
[34] Noronha J, Qian M, Leary M, Kyriakou E, Brudler S, Brandt M. Manufacturability of Ti-6Al-4V hollow-walled lattice struts by laser powder bed fusion. JOM 2021;73:4199–208. https://doi.org/10.1007/s11837-021-04914-5.
[35] Afdhal, Jirousek O, Palar PS, Falta J, Dwianto YB. Design exploration of additively manufactured chiral auxetic structure using explainable machine learning. Mater Des 2023;232:112128. https://doi.org/10.1016/j.matdes.2023.112128.
[36] Zhang J, Lu G, Wang Z, Ruan D, Alomarah A, Durandet Y. Large deformation of an auxetic structure in tension: experiments and finite element analysis. Compos Struct 2018;184:92–101. https://doi.org/10.1016/j.compstruct.2017.09.076.
[37] Zhang WM, Li ZY, Yang JS, Ma L, Lin Z, Schmidt R, Schröder KU. A lightweight rotationally arranged auxetic structure with excellent energy absorption performance. Mech Mater 2022;166. https://doi.org/10.1016/j.mechmat.2022.104244.
[38] Wang X-T, Wang B, Li X-W, Ma L. Mechanical properties of 3D re-entrant auxetic cellular structures. Int J Mech Sci 2017;131–132:396–407. https://doi.org/10.1016/j.ijmecsci.2017.05.048.
[39] Gärtner T, van den Boom SJ, Weerheijm J, Sluys LJ. Geometric effects on impact mitigation in architected auxetic metamaterials. Mech Mater 2024;191:104952. https://doi.org/10.1016/j.mechmat.2024.104952.
[40] Novak N, Vesenjak M, Krstulović-Opara L, Ren Z. Mechanical characterisation of auxetic cellular structures built from inverted tetrapods. Compos Struct 2018;196:96–107. https://doi.org/10.1016/j.compstruct.2018.05.024.